PAUL SCHERRER INSTITUT

December 1996 Version 2

THE RADIATION ENVIRONMENT MONITOR

SCIENTIFIC DATA EXTRACTION

Part I

ESTEC/Contract No. 11108/94/N1/JG(SC)
WP 33, 331, 332

P. Bühler
Paul Scherrer Institute
CH–5232 Villigen PSI, Switzerland

Contents

1 Introduction

Since the first switch–on in space of the REM instrument aboard the UK STRV–1B satellite in June 1994, roughly 150000 observations have been made until the end of November 1996. For each of these observations REM delivered two histograms containing number of counts accumulated over a certain time. These counts have been triggered by incident particles (protons, electrons) with different energies and by electronic noise. The counts caused by various effects are all mixed together and are a priori not distinguishable from each other.

The goal of the scientific data extraction task is to extract from the accumulated REM histograms as much information on the incident particles, their species and energy spectrum, as possible. Therefore the involved physical processes of the particle interaction with the detector and the working scheme of the detector electronics have to be understood and taken into account.

This document describes the applied procedures. It assumes the reader to be familiar with the basics of the REM instrument (for an introduction to REM and its behaviour in space see [**?**]). The developed procedures are based on the data taken until end of November 1996.

In section 2 some detector principles are discussed which are important for the understanding of the measurements. In section 3 the applied data treatment is explained step by step in detail and demonstrated on various examples.

2 Detector principles

2.1 Geometric parameters

The geometric parameters of the STRV–REM detectors are listed in table 1. Note that the sensitive area of the e–detector is 50 $[mm^2]$, two times the size it was thought to be before launch!

Table 1: Properties of REM detectors aboard the STRV–satellite.

Detector	Sensitive detector area [mm^2]	Thickness of silicon diode [μm]	Shielding [mm, material]
p	150	298	3.0, aluminium
			0.75, tantalum
e	50	310	3.0, aluminium

2.2 Energy deposit

REM measures the charge produced by particles penetrating silicon detectors. In an unshielded silicon detector the amount of deposited energy E_{dep} depends on the type of particle, incident particle energy E_{ind}, and path length dx in the detector. The differential energy loss dE/dx(E) in silicon has been measured for protons [1] and electrons [2]. They are shown in figure 2.2 for the REM relevant energy range.

Particle incident energy and deposited energy are related by

$$E_{dep} = dE/dx(E_{ind}) \cdot dx \tag{1}$$

In a real case, like REM however, this simple relation between the particles incident energy and the energy deposited in the diode is falsified by various effects. The main entrance window of the REM detectors is defined by a cone with a half opening–angle of 45°. However, particles with sufficient energy are able to traverse the STRV satellite and can therefore be detected from all sides. As a consequence the path length dx of the particles in the diode is not a fixed size. The particles have to pass the surrounding shielding material where they lose energy. As the effective thickness of the shielding is not spherically symmetric the energy loss is a function of the angle of incidence.
It is therefore possible that two particles of different energy and with different angles of incidence can deposit the same amount of energy in the silicon diode. This limits the accuracy with which incident energies can be deduced from measured deposited energies.

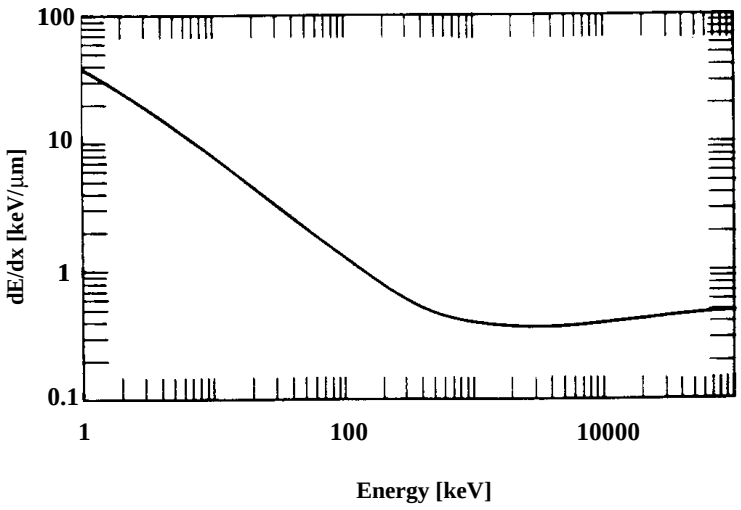

(a)

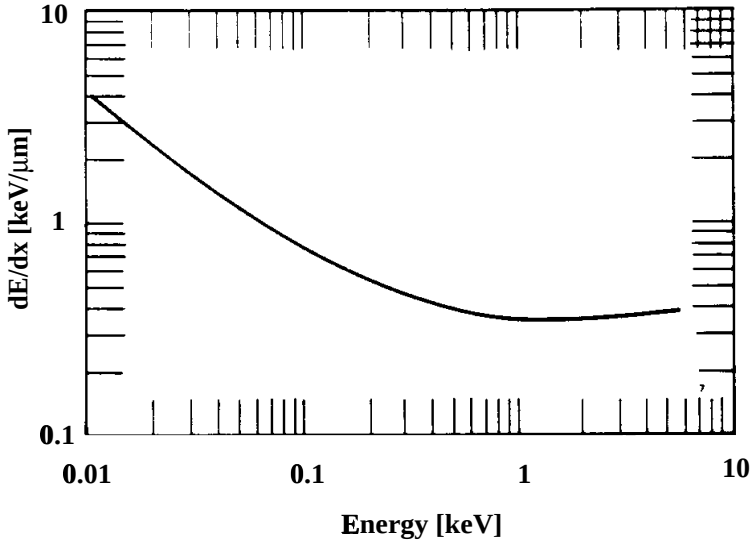

(b)

Figure 1: Differential energy transfer dE/dx for (a) protons [1] and (b) electrons [2] in silicon.

2.3 Event detection and counting

The charge produced in the diodes by penetrating particles is amplified by a charge sensitive amplifier and converted into a voltage pulse. The amplitude of the resulting signal is proportional to the deposited energy and is measured with a 12 bit ADC. The 4095 ADC channels are binned into 16 detector channels using the algorithm given in table 2. Data is successively accumulated during a period of time t_{acc} of typically 100 sec. For each accumulation time two 16-bin histograms result, containing the accumulated number of counted events.

Table 2: Histogram compression function applied in the STRV–REM detectors. The deposited energies are given in MIPS of protons (1 MIP = 1.6 $[MeV \cdot cm^2 \cdot g^{-1}]$).

Histogram bin	ADC output range	Deposited energy [MIPS] p–detector	Deposited energy [MIPS] e-detector
1	1	0.5 – 0.7	0.2 – 0.4
2	2	0.7 – 1.0	0.4 – 0.7
3	3 – 6	1.0 – 1.9	0.7 – 1.6
4	7 – 8	1.9 – 2.4	1.6 – 2.1
5	9 – 10	2.4 – 2.8	2.1 – 2.5
6	11 – 12	2.8 – 3.3	2.5 – 3.0
7	13 – 15	3.3 – 4.0	3.0 – 3.7
8	16 – 19	4.0 – 5.0	3.7 – 4.6
9	20 – 23	5.0 – 5.9	4.6 – 5.6
10	24 – 30	5.9 – 7.6	5.6 – 7.2
11	31 – 42	7.6 – 10.4	7.2 – 10.0
12	43 – 79	10.4 – 19.1	10.0 – 18.6
13	80 – 275	19.1 – 65.3	18.6 – 64.2
14	276 – 727	65.3 – 171.4	64.2 – 169.7
15	728 – 4000	171.4 – 942.6	169.7 – 934.0
16	4001 – 4095	> 940	> 930

2.3.1 Pile–up rejection

In order to prevent the signals of two succeeding events to pile–up, after each detection of an event the detector is enabled to accept a next event for a time τ which is roughly 23 μs. The enabling time is updated by each new detection which causes at very high detection rates the detector to be completely "closed".

In the following we must distinguish between detected events and counted events. An event is detected when its signal exceeds the detection threshold $V_{th_{det}}$. Each detected event triggers the pile–up prevention mechanism. Besides real events also noise can cause detections and the triggering of the pile–up rejection mechanism. The rate of detected events will be denoted with n_{det}. In order to be counted an event must be detected and its signal must exceed the lower threshold V_{th_1} of detector channel 1. The count rate in channel i will be denoted by n_i and the total count rate by n_{count}.
In fact V_{th_1} should be lower than $V_{th_{det}}$ such that all detected events are counted. However, if $V_{th_{det}} < V_{th_1}$ there is a number of detected events which are not counted. Their rate shall be denoted by n_0.

2.4 Deadtime

Each detection enables the detector for a certain period to count succeeding events. The number of detected events absorbed by this pile–up rejection mechanism n_{rej} increases with growing detection rate and is given by

$$n_{rej} = n_{det} \cdot (1 - e^{-n_{det} \cdot \tau}) \tag{2}$$

The deadtime t_D is the fraction of time the detector is enabled and is given by

$$\begin{aligned} t_D &= \frac{n_{rej}}{n_{det}} \\ &= (1 - e^{-n_{det} \cdot \tau}) \end{aligned} \tag{3}$$

The deadtime corrected count rate $n_{i_{dtc}}$ is the total rate of detections having signal amplitudes large enough for the event to be counted in detector channel i. $n_{i_{dtc}}$ is obtained by multiplication of the measured rate with the correction factor $1/(1 - t_D)$

$$n_{i_{dtc}} = \frac{n_i}{1 - t_D} \tag{4}$$

2.5 Test pulser

A built–in test pulser allows to artificially induce charge pulses at the input of the preamplifiers at a predefined rate. It is regularly switched on for a certain period and can be used to check the proper functioning of the detector and to measure the deadtime. The nominal count rate of the testpulser at vanishing deadtime n_{tp} has been calibrated before launch [3] and has been shown to be a function of the detector temperature $T4$ (figure 2.5). The total minimal testpulser count rate at room temperature is roughly 2000 $[Hz]$ and the temperature slope is -3.4 $[Hz/°C]$.

The testpulser histograms have a characteristic shape which has also been measured [3] and is shown in figure 2.5. The distribution is the same for both detectors. Comparison of in–flight measured test histograms with this calibration histogram allows to check the proper functioning of the detector electronics.

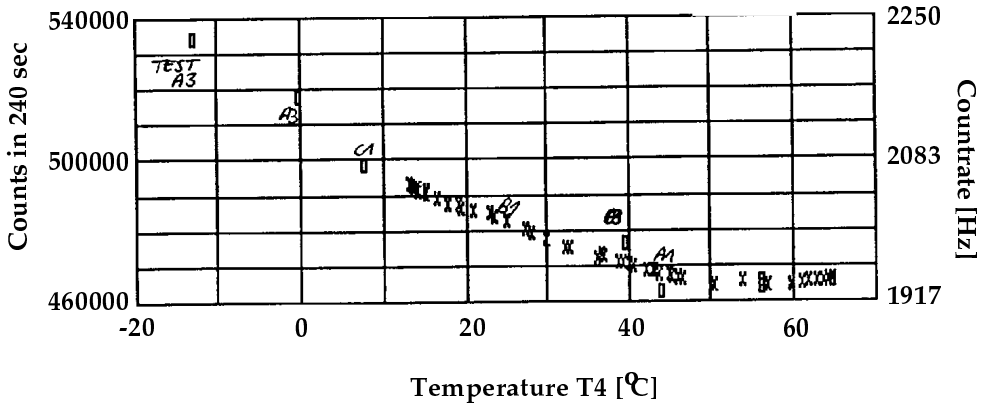

(a)

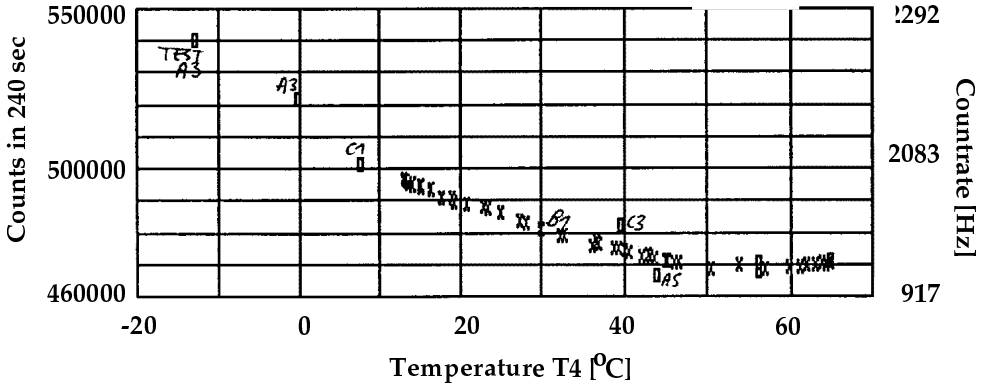

(b)

Figure 2: Calibrated temperature dependence of the nominal testpulser count rate n_{tp} in (a) p–detector and (b) e–detector [3].

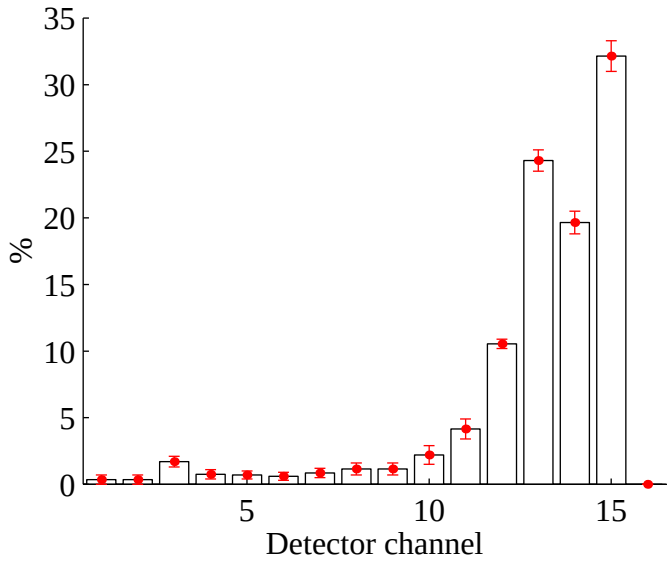

Figure 3: Calibrated distribution of the testpulser histograms.

During the testpulser is switched on the electronic logics allows real events to be detected but not to be counted. Only testpulser events are counted. Thus the testpulser count rate is affected by the deadtime caused by the real event detection rate. The count rate $n_{tp_{count}}$ of the testpulser events is

$$n_{tp_{count}} = n_{tp} \cdot (1 - t_D) \tag{5}$$

Measuring $n_{tp_{count}}$ and knowing n_{tp} the deadtime t_D can be deduced from relation (5).

2.6 Detector response

As discussed above the amount of energy E_{dep} deposited in the silicon diode by a penetrating particle is a function of the particles incident energy E_{inc}, the shielding geometry, the angle of incidence α, and the particle species k (p, e, ions) ($E_{dep}(E_{inc}, \alpha, k)$). Together with the binning algorithm described in table 2 the energy response of the detector, the relation between incident particle flux and count rates per detector channel, is defined.

2.6.1 Geometric factors

The energy response of each REM detector can be expressed by its geometric factors per histogram bin $G_k(E, \alpha, i)$. $G_k(E, \alpha, i)$ is an area, expressed in cm^2, which's size is proportional to the probability for an incident particle of species k with energy E and angle of incidence α to be detected in detector channel i. In the following the index i will run from 1 to 32, where channels 1 to 16 are the p-detector channels and channels 17 to 32, the e-detector channels.

The deadtime corrected count rates are related to the proton and electron fluxes (f_p and f_e) and the geometric factors of the instrument by

$$n_{i_{dtc}} = \int_0^\infty dE \cdot f_p(E, \alpha) \cdot G_p(E, \alpha, i) + \int_0^\infty dE \cdot f_e(E, \alpha) \cdot G_e(E, \alpha, i) \tag{6}$$

where f_k is given in $Hz \cdot MeV^{-1} \cdot cm^{-2}$.

Note that in this approach the contribution of ions is neglected. Ions are supposed to contribute only to the high detector channels and as the observations show that the count rates in these channels are very low their neglection is justified.

Equation (6) describes the fundamental relation between the incident particle fluxes and the detector count rates and will be used to deduce the particle spectra from the measured data.

In equation (6) the particle fluxes are a function of the angle of incidence. As REM does not allow to measure α we will assume for the rest of this document the particle fluxes to be isotropically distributed in space. Thus the used geometric factors are reduced to $G_k(E_{inc}, i)$.

The geometric factors were determined by extensive numerical simulations of the complete instruments including carrying satellite [4]. The results for the STRV–REM are given in tables 3 to 6 and are plotted in figure 2.6.1.

The tables are composed of 19 columns. The first column (E) is the particles incident energy in MeV. The values in column two (Frac) represent the detection probability for a particle with

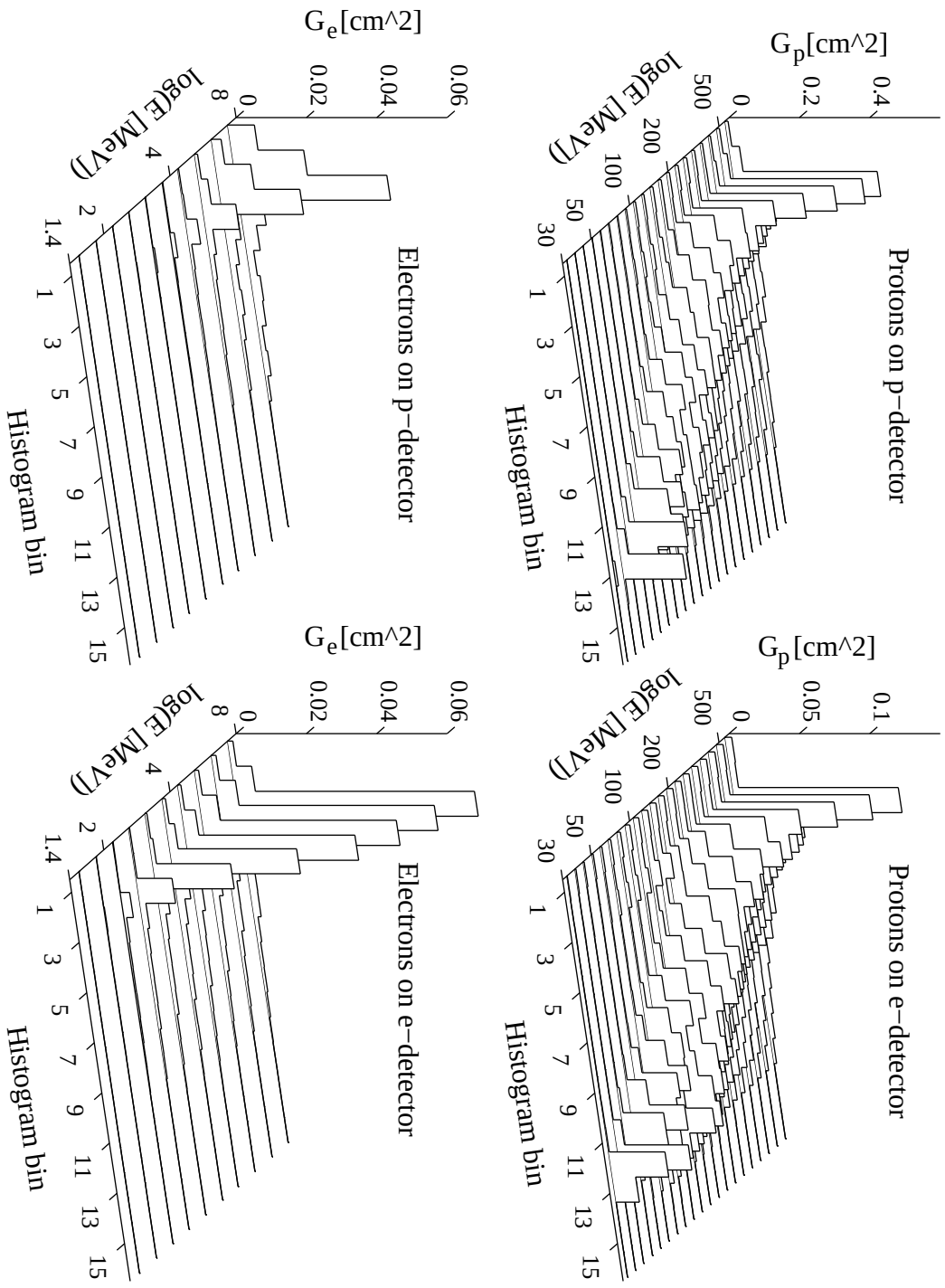

Figure 4: Geometric factors as function of incident particle energy for protons and electrons on the two STRV–REM detectors.

energy E. The incident particle flux per cm^2 divided by Frac gives the total count rate. Columns 3 to 18 (p_i) contain the percentage of the count rate in the different detector channels. The last column (Cnts) is the total number of simulated events which have resulted in a count. The geometric factors for the simulated energies E_{sim} are given by

$$G_k(E_{sim}, i) = \frac{p_i}{100 \cdot Frac} \tag{7}$$

2.6.2 Error analysis: geometric factors

We calculate the errors of the geometric factors applying simple error propagation to equation (7).

$$\Delta^2 G_k(E_{sim}, i) = (\frac{\Delta p_i}{100 \cdot Frac})^2 + (\frac{p_i \cdot \Delta Frac}{100 \cdot Frac^2})^2 \tag{8}$$

With

$$p_i = \frac{Cnts_i}{Cnts} \cdot 100$$

and

$$Frac = \frac{N_{sim}}{Cnts}$$

where N_{sim} is the number of simulated incident particles per cm^2. Using $\Delta Cnts_i^2 = Cnts_i$, $\Delta^2 Cnts = Cnts$, and $\Delta N_{sim} = 0$ one gets

$$\Delta G_k(E_{sim}, i)^2 = \begin{cases} \frac{G_k(E_{sim},i)^2}{Cnts} \cdot \left(2 + \frac{1}{G_k(E_{sim},i) \cdot Frac}\right); & p_i \neq 0 \\ (\frac{1}{Cnts \cdot Frac})^2; & p_i = 0 \end{cases} \tag{9}$$

The such calculated error only takes into account the uncertainties caused by the statistical nature of the Monte Carlo simulation. Thus some of the errors are very small. The systematic errors caused by the simplified geometry of the satellite and detector model structures are difficult to estimate. However, in order to account for it the errors are multiplied by a factor 2. Then the relative error of each factor is assumed to be at least 10%. Thus whenever the resulting relative error comes out to be less than 10% it is set to 10%.

Table 3: STRV–REM p–detector response to protons (see text for a discussion of the different columns).

Table 4: STRV–REM p–detector response to electrons (see text for a discussion of the different columns).

Table 5: STRV–REM e–detector response to protons (see text for a discussion of the different columns).

Table 6: STRV–REM e–detector response to electrons (see text for a discussion of the different columns).

3 Data reduction

The reduction of the accumulated REM histograms is done in two main steps: first the count rates are corrected for deadtime effects and second the information on the energy spectra of the incident protons and electrons is extracted.

3.1 Deadtime correction

In this first step the deadtime t_D and the deadtime corrected count rates $n_{i_{dtc}}$ are computed. Combination of equation (2) and relation $n_{det} - n_{rej} = n_{count} + n_0$ leeds to the following expression

$$n_{count} + n_0 = n_{det} \cdot e^{-n_{det} \cdot \tau} \tag{10}$$

Note that the value of $n_{count} + n_0$ has a maximum of $e^{-1} \cdot \tau^{-1} \approx 16000$ for $n_{det} = 1/\tau \approx 44000$. At detection rates larger than $1/\tau$ deadtime becomes important such that the count rate decreases with increasing detection rate.

In the case where $n_0 = 0$, n_{det} can be deduced from equation (10) and using equation (4) the deadtime t_D can be calculated. However, for each n_{count} there are two solutions for n_{det}, one below and one above the value $1/\tau$. The real value can only be selected by analyzing a series of contiguous measurements assuming the detection rate to develop smoothly in time.

In the case where $n_0 \neq 0$, n_0 is an additional unknown and the single equation (10) is not sufficient to compute n_{det}. In this case the testpulser measurements must be used to determine the deadtime (equation (5)) and (4) to calculate the deadtime corrected count rates.

In fact the relevant thresholds $V_{th_{det}}$ and V_{th_1} in the STRV–REM detectors have been adjusted such that n_0 should vanish. However, there is strong evidence that at least for the p–detector the thresholds must have shifted with time such that n_0 can not be neglected. This is illustrated in figure 3.1 where real event count rates and testpulser count rates taken on 27 January 1995 are plotted versus time. In the case of $n_0 = 0$ the testpulser count rate is expected to be maximal when the real event count rate is low and to decrease with increasing event count rate as is observed in the e–detector. In the p–detector the testpulser count rates do not behave as expected. They are also low when the real event count rates are low which is an indication for an important amount of detected, but not counted events.

Thus the testpulser accumulations are used to deduce the deadtime (equation (5)) and equation (4) to calculate the deadtime corrected count rates.

3.1.1 Testpulser count rate

Equation (5) is only valid if it can be assumed that during testpulser accumulations only testpulser events are counted. Unfortunately the real event rejection mechanism seems to be leaky such that the low detector channels are significantly contaminated by real events. This is shown in figure 3.1.1 where in the uppermost panel the real count rate and in the following panels the testpulser count rates in the different channels are plotted versus time. The exemplary data shown has been taken on 5 October 1994. The testpulser count rate curves in the lower detector channels follow the real event count rates and thus are clearly contaminated by real events.

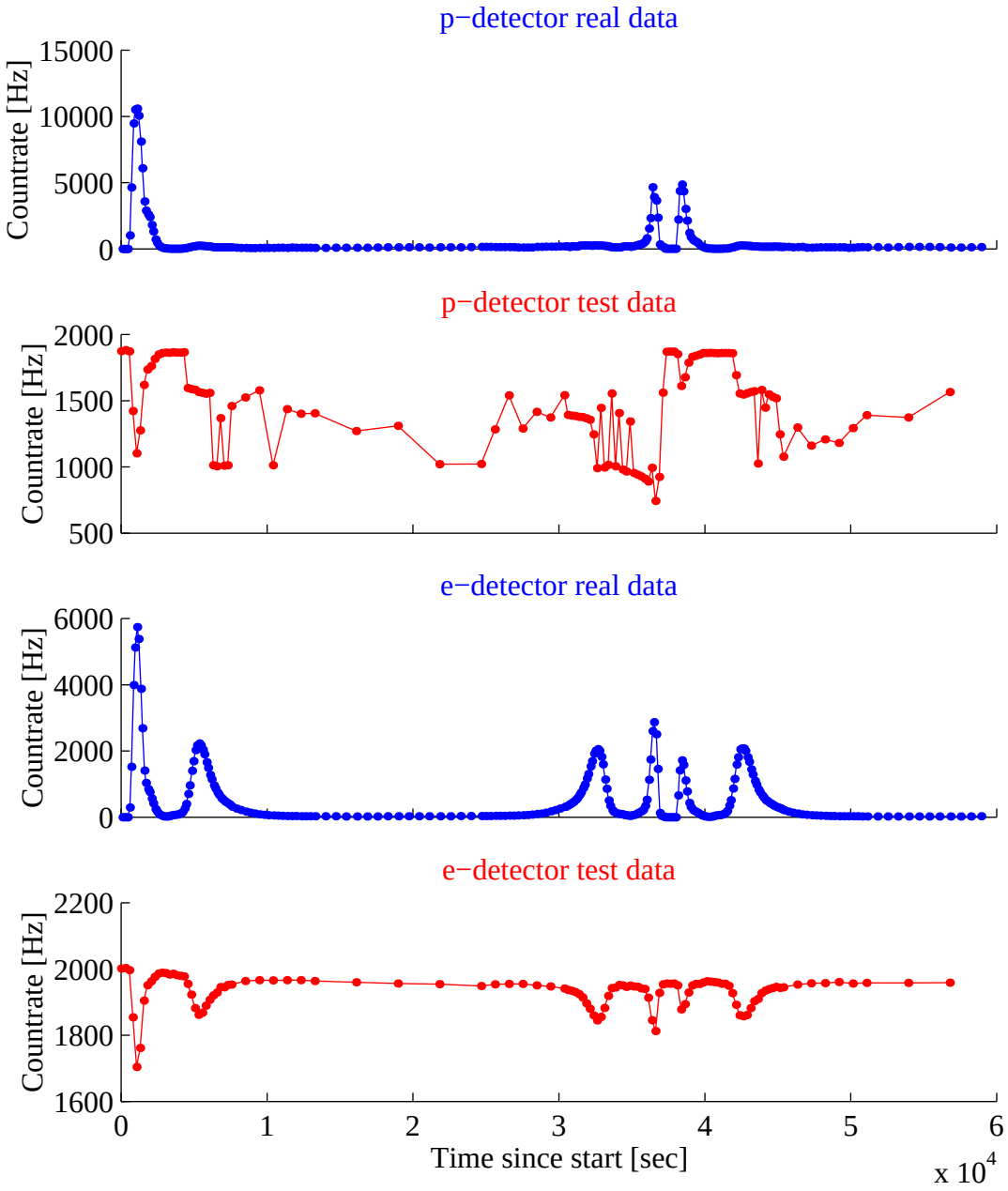

Figure 5: STRV–REM real and testpulser count rates on 27 January 1995 demonstrating the importance of non–counted events contributing to the deadtime in the p–detector. The testpulser count rate should be maximal when the real event count rate is low and should decrease with increasing event count rate as is observed in the e–detector. The disturbed behaviour of the testpulser count rate in the p–detector indicates an important amount of detected, but not counted events (n_0).

Channels 13 to 15 contain more than 60% of the counts and look rather "clean". The same plots for 1 November 1996 are shown in figure 3.1.1. Also here the low channels are contaminated but channels 13 to 15 look "clean".

Thus **only detector channels 13 to 15 are used for deadtime calculation** and are assumed to be free of contamination by real events.

3.1.2 Nominal testpulser count rate

The nominal testpulser count rate n_{tp} of equation (5) is a function of temperature (figure 2.5) and has also changed during the mission. In figure 3.1.2 the count rates of all testpulser accumulations of the e–detector are plotted versus time. The different colors indicate the detector temperature $T4$. A low testpulser count rate indicates a large deadtime and a high testpulser count rate, a low deadtime. For the largest testpulser count rates at a given time the deadtime is assumed to be negligible. Thus the curve drawn by the uppermost points in figure 3.1.2 represents the nominal testpulser count rate n_{tp} as function of time.

Its value has dramatically changed during the mission. Three domains can be distinguished. Until February 1996 the testpulser rate has steadily increased. After January 1996 the rate jumped from around 2200 Hz to over 3500 Hz. The jump occurred first at low temperatures and then successively also at higher ones. After September 1996 the testpulser rate started to drop to 0, again first at low temperatures and later at higher temperatures too.

The temperature slope at all times was negative. The highest testpulser count rates have been measured at low temperatures, in agreement with the calibration measurements. However, the temperature slope has also change during the mission.

In order to describe the nominal testpulser count rate $n_{tp}(T4, t)$ as a function of temperature $T4$ and OBC time t (OBC time is the number of seconds elapsed since start of year 1992) it is parametrized as follows

$$n_{tp}(T4, t) = [a(t) + b(t) \cdot (t - t_{i_{min}})] + c(t) \cdot T4 \tag{11}$$

$a(t)$ and $b(t)$ are piecewise constant in time intervals $t_{i_{min}}, t_{i_{max}}$.

The temperature factor c measured before launch was found to be -3.4 $[Hz/^{\circ}C]$ for both detectors. This value has also changed since start. In figure 3.1.2 the maximum testpulser count rates are plotted as function of temperature $T4$ at several different dates.

At the beginning the resulting temperature slope is compatible with the calibrated value. With increasing time (from bottom to top (blue to red)) the temperature slope decreased. The slopes $c(t)$ of the lines drawn in the figure have been calculated using the following relations

$$c(t) = \begin{cases} -3.4, & t \leq 8.4 \cdot 10^7 \\ -3.4 - 1.4506 \cdot 10^{-7} \cdot (t - 8.4 \cdot 10^7) & t > 8.4 \cdot 10^7 \\ -24.0 & t > t_{\nearrow}(T) \end{cases} \tag{12}$$

The temperature slope of the enhanced testpulser rates is approximated by -24.0.

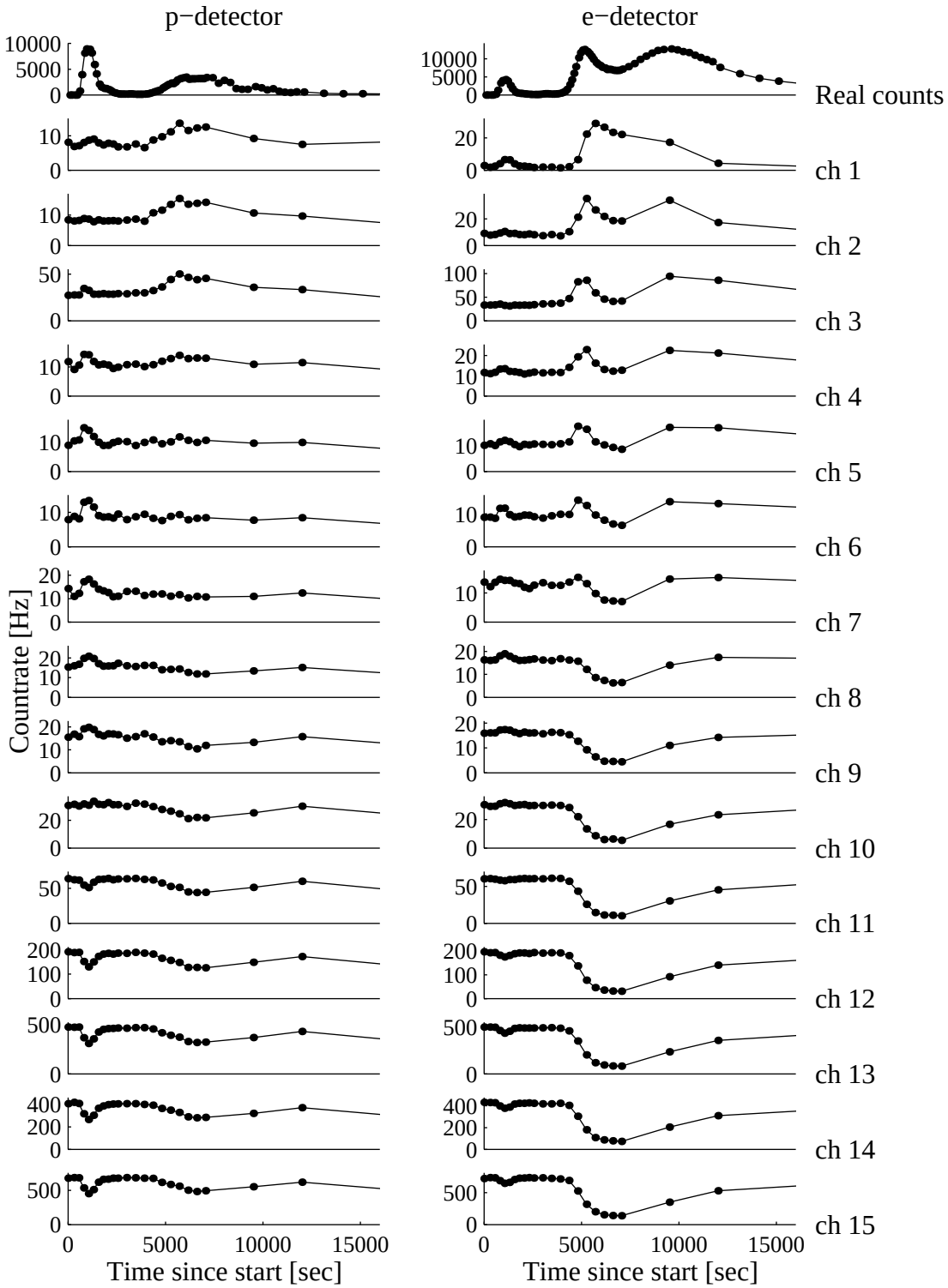

Figure 6: STRV–REM count rates per detector channel on 5 October 1994 demonstrating the contamination of the testpulser accumulations by real events. In the uppermost panel the real count rates and in the following panels the testpulser count rates in the different detector channels are plotted versus time. The count rate curves in the lower detector channels follow the real event count rates and thus are clearly contaminated by real events. Channels 13 to 15 look rather clean and thus are used for deadtime determination.

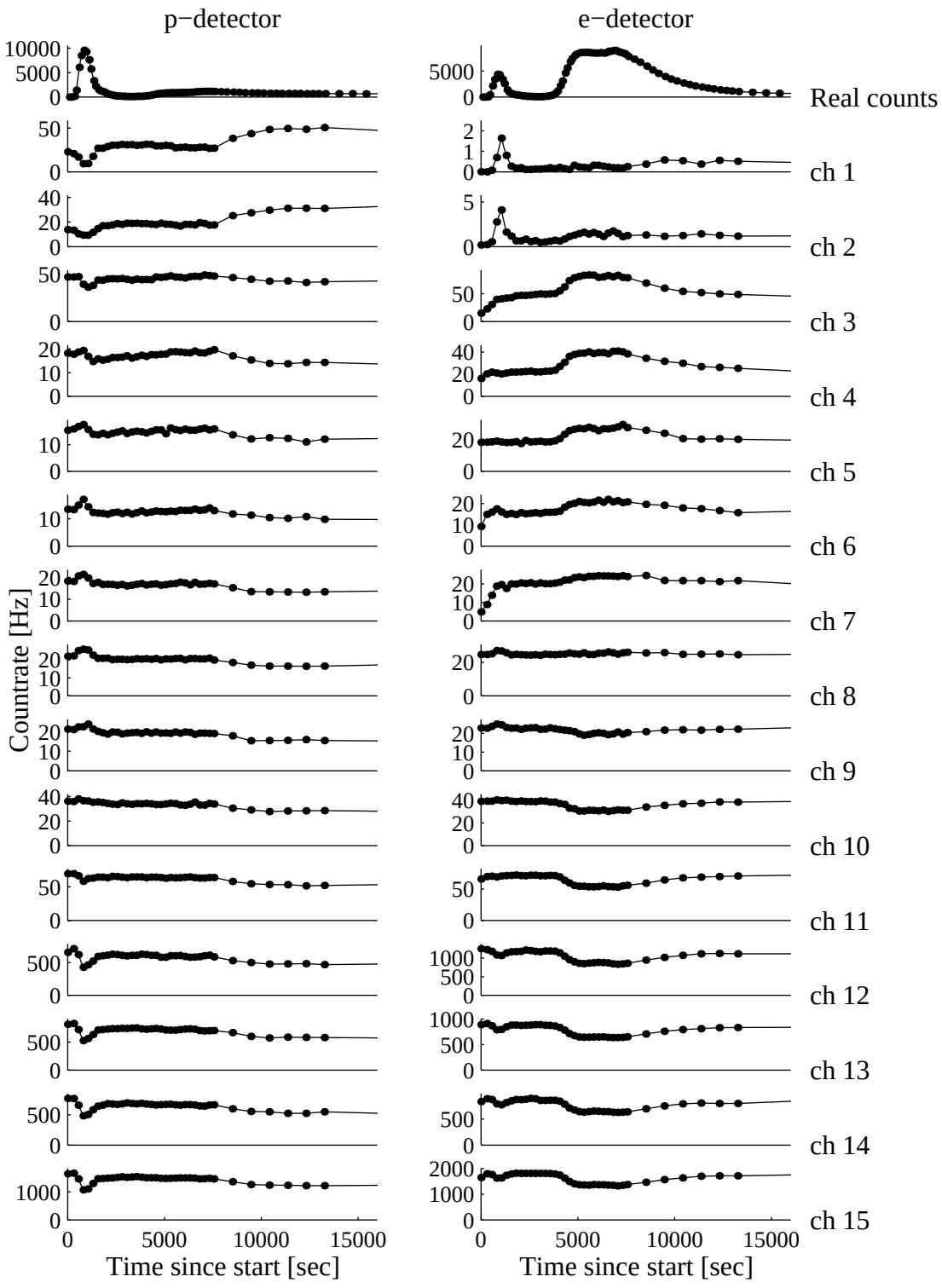

Figure 7: Same as figure 3.1.1 on 1 November 1996.

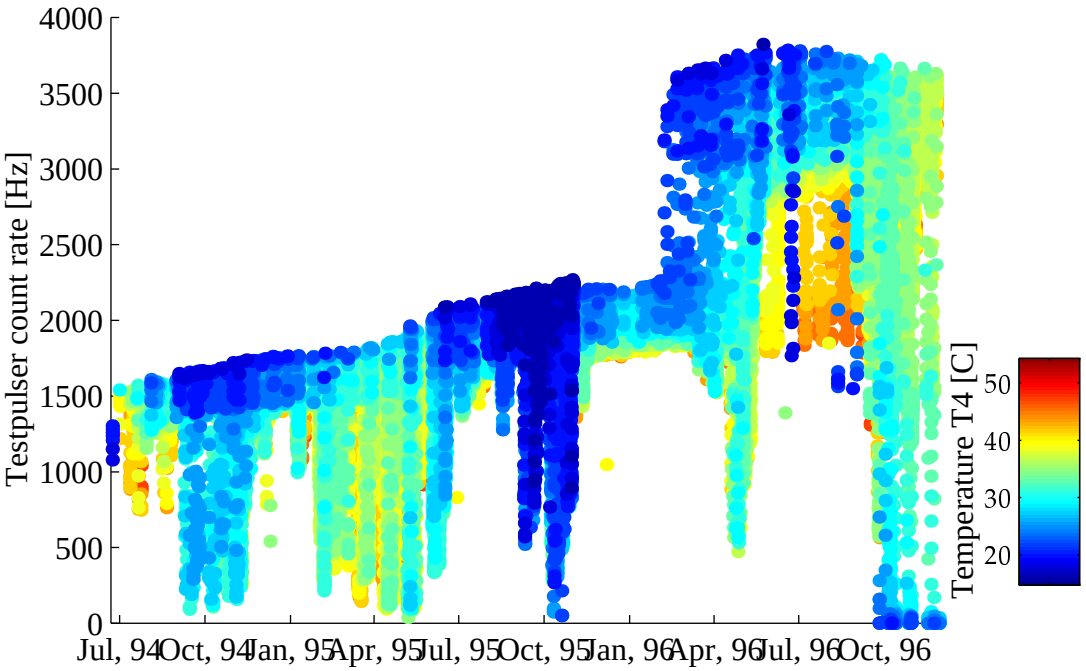

Figure 8: Measured testpulser count rates as function of time and detector temperature $T4$. The curve drawn by the uppermost points represents the nominal testpulser count rate n_{tp} as function of time. Its value has dramatically changed since the start.

The values used for a, b and the time intervals $t_{i_{min}}, t_{i_{max}}$ are given in table 7. "Normal rates" are rates before the jump to higher values and "high rates", the rates after.

The times when the testpulser rate jumped to high rates ($t_{\nearrow}$) and to 0 ($t_{\searrow}$) depend on the detector temperature $T4$. They are given in table 8.

Figure 3.1.2 shows this approximation of the testpulser nominal count rate in the e–detector for the time from July 1994 to November 1996 for a series of temperatures. The lines have been calculated with equations (11) and (12) and the parameter values given in tables 7 and 8. The dots are testpulser count rates for which the real event count rate is less than 1000 $[Hz]$, thus testpulser accumulations for which deadtime can be assumed to be small.

Due to the non–negligible n_0 in the p–detector the same analysis can not be applied for this detector. From calibration we know that the nominal testpulser count rates of the p and e–detector have been approximately equal. We assume that the testpulser count rates have developed similarly in both detectors thus the same approximation is used for the p–detector nominal testpulser count rate.

In order to make the deadtime correction of the real event count rates the factor $(1 - t_D)$ is calculated for the testpulser accumulations with equation (5). Then this factor is linearly interpolated for times of real data accumulations ($(1 - t_D)_{interp}$). These values are then used to calculate the deadtime corrected count rates with equation (4).

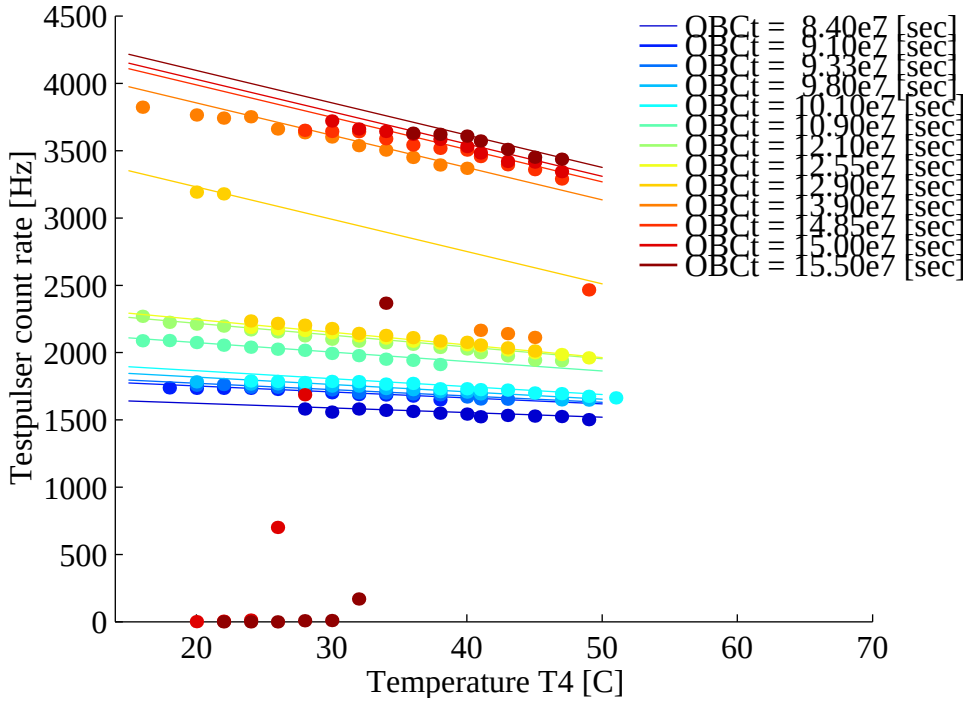

Figure 9: Temperature dependence of the nominal testpulser rate measured at different times. The temperature slope has increased (more negative) since the start. Note the jump to increased rates after t=$12.9 \cdot 10^7$ (February 1996) and the drop to 0 starting first at low temperatures after t=$14.85 \cdot 10^7$ (15 September 1996).

Table 7: Set of parameters for the parametrization of the nominal testpulser rate $n_{tp}(T4, t)$ of the e-detector using equation (11).

Normal rates				High rates			
$t_{i_{min}}$	$t_{i_{max}}$	a	b	$t_{i_{min}}$	$t_{i_{max}}$	a	b
10^7 [sec]		[Hz]	[Hz^2]	10^7 [sec]		[Hz]	[Hz^2]
7.90	8.40	1692	0	12.90	13.00	3709	$31.468 \cdot 10^{-5}$
8.40	9.10	1692	$1.959 \cdot 10^{-5}$	13.00	13.20	4024	$5.578 \cdot 10^{-5}$
9.10	9.33	1829	$1.068 \cdot 10^{-5}$	13.20	14.00	4135	$2.855 \cdot 10^{-5}$
9.33	9.80	1854	$1.275 \cdot 10^{-5}$	14.00	14.50	4364	$0.601 \cdot 10^{-5}$
9.80	10.10	1914	$2.231 \cdot 10^{-5}$	14.50	15.00	4394	$2.232 \cdot 10^{-5}$
10.10	10.90	1981	$2.786 \cdot 10^{-5}$	15.00	–	4505	$2.405 \cdot 10^{-5}$
10.90	12.10	2203	$1.415 \cdot 10^{-5}$				
12.10	12.55	2373	$1.023 \cdot 10^{-5}$				
12.55	12.90	2419	$1.315 \cdot 10^{-5}$				
12.90	–	2465	$1.525 \cdot 10^{-5}$				

Table 8: $t_{\nearrow}$ and $t_{\searrow}$ as function of temperature $T4$. The times are seconds elapsed since 1 January 1992, 00:00:00.

$T4$	$t_{\nearrow}$	$t_{\searrow}$
	$[10^7\ sec]$	
16	12.576	14.0
18	12.699	14.0
20	12.945	14.1
22	12.945	14.5
24	13.027	14.9
26	13.247	14.9
28	13.392	14.9
30	13.497	15.0
32	13.649	15.0
34	13.675	15.2
36	13.679	15.2
38	13.731	> 15.2
40	13.928	–
41	13.999	–
43	14.235	–
45	14.502	–
47	14.647	–
49	14.915	–
51	> 14.915	–

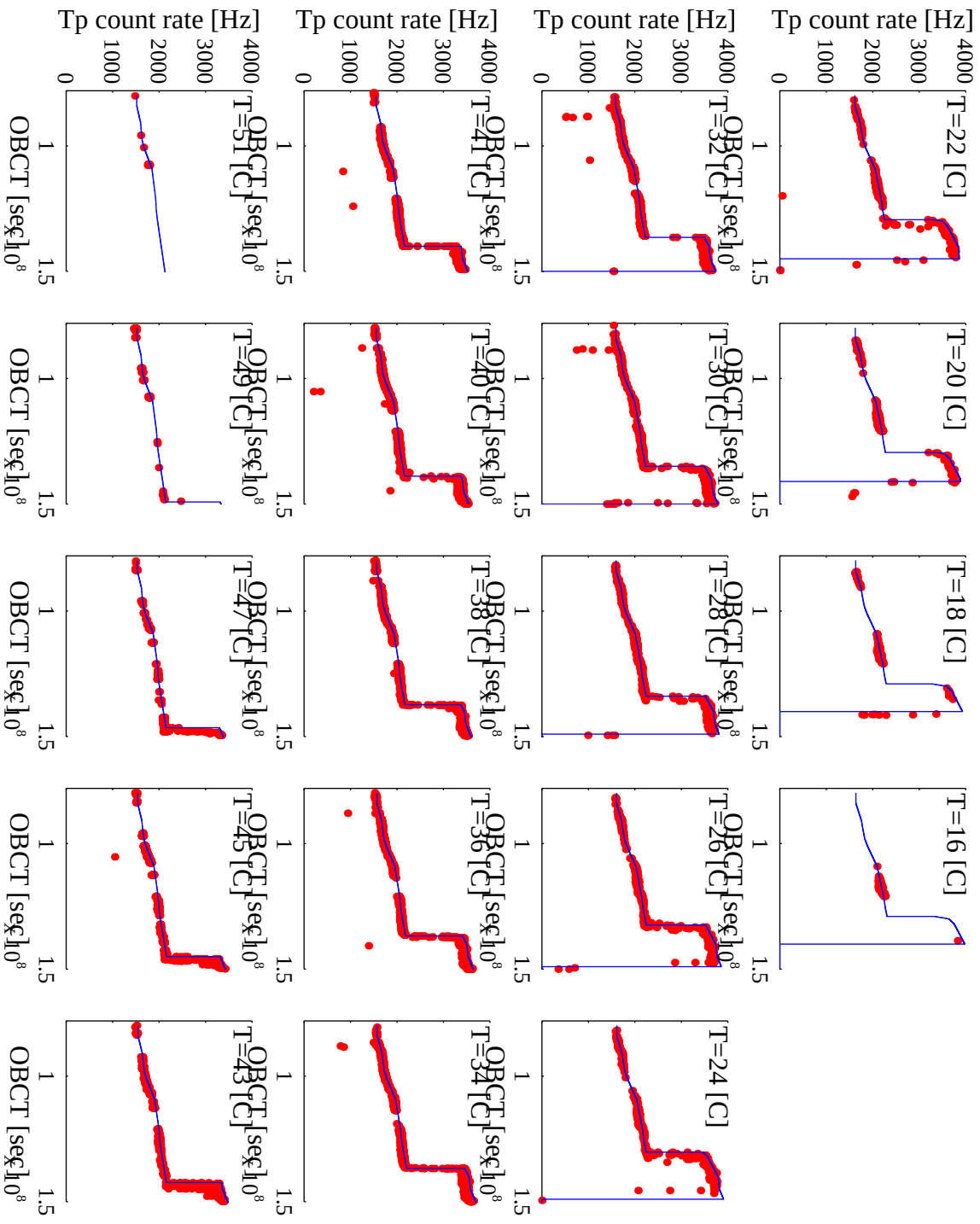

Figure 10: Parametrization of the nominal testpulser count rate as function of time and detector temperature $T4$. The dots are measured testpulser rates for which deadtime could be assumed to be small, thus representing the nominal testpulser count rate. The approximating bold lines have been calculated with equations (11) and (12) using the parameters given in tables 7 and 8.

3.1.3 Noise contamination

The electronic noise level can surpass the counting threshold V_{th_1} and lead to noise contamination. It is the lowest detector channels which are affected most. In figure 3.1.3 the count rates in channel 1 to 5 of both detectors are plotted versus time for three different observations made on June 30, 1994, April 13, 1995, and August 31, 1995, respectively. Blue curves (upper panels) are p–detector rates and red curves (lower panels), e–detector rates.

The data taken on 30 June 1994 was one of the first observations. All e–detector channels look completely clean. The first channel of the p–detector has an increased rate during the passes of the outer radiation belt. The shape of the count rate curve however follows the features in the e–detector channels. Thus the counts in the lowest p–detector channel are very likely caused by electrons producing bremsstrahlung in the tantalum shielding of the p–detector.
On 31 August 1995 the first channel of both detectors are dominated by events which are not related to real events. On 25 November 1996 the first two channels are completely swamped by noise events. Whereas in 1994 and 1995 there is no indication for a significant contamination of detector channels 3 and higher, an enhanced count rate in channels 3 of the November 1996 data is noted.

3.1.4 Error analysis: deadtime correction

The error of the deadtime corrected count rates $\Delta n_{i_{dtc}}$ can be written as (see equations (4) and (5))

$$\Delta^2 n_{i_{dtc}} = n_{i_{dtc}}^2 \cdot \left(\left(\frac{\Delta n_i}{n_i} \right)^2 + \left(\frac{\Delta (1 - t_D)_{interp}}{(1 - t_D)_{interp}} \right)^2 \right) \tag{13}$$

The error of the count rates $\Delta^2 n_i$ is n_i (statistical error). $\Delta(1 - t_D)_{interp}$ is a linear combination of the errors of the values of $\Delta(1 - t_D)$ determined for the testpulser accumulations and used for interpolation of $1 - t_D$. $\Delta(1 - t_D)$ is

$$\Delta^2 (1 - t_D) = (1 - t_D)^2 \cdot \left(\left(\frac{\Delta n_{tp_{count}}}{n_{tp_{count}}} \right)^2 + \left(\frac{\Delta n_{tp}}{n_{tp}} \right)^2 \right) \tag{14}$$

where $\Delta^2 n_{tp_{count}}$ is $n_{tp_{count}}$ (statistical error) and the relative error of the nominal testpulser count rate $\Delta n_{tp}/n_{tp}$ of the e–detector is assumed to be 5% and that of the p–detector, 10%.

In order to account for the additional error of the count rates due to noise contributions we multiply the count rate errors (Δn_i) of each detector channel with an individual weighting factor. These factors are given in table 9

As the first two channels can be totally swamped by noise events, only channels 3 to 16 are used for total count rate calculations.

3.1.5 Results

In order to check the deadtime correction a criterion for the quality of the corrected data is needed. A coarse test is the following: consider two contiguous passages of the REM instrument

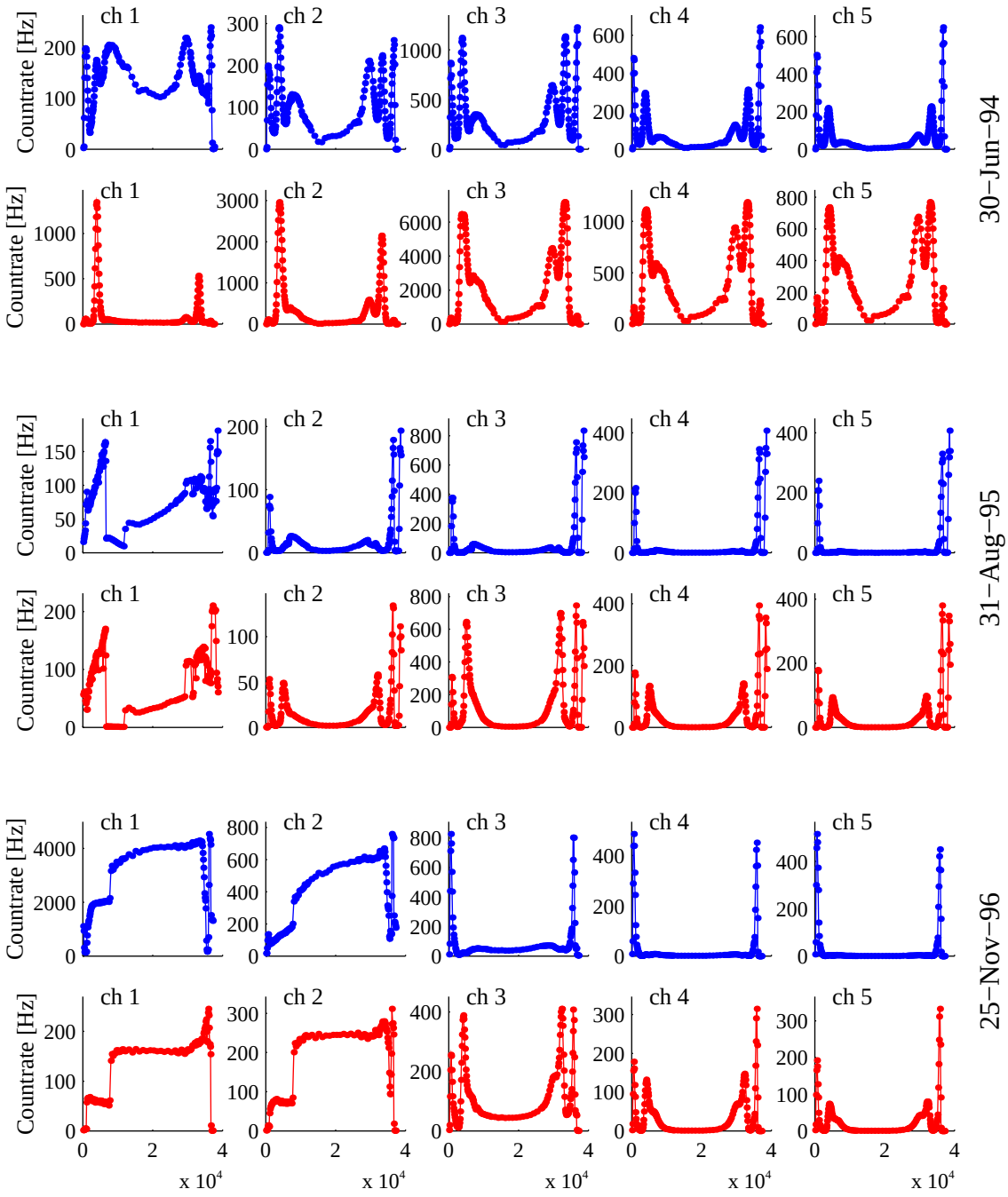

Figure 11: STRV–REM count rates in detector channels 1 to 5 on (t.t.b.) 30 June 1994, 31 August 1995, and 25 November 1996 demonstrating the contamination of the count rates in the lowest channels by noise events. The two panels per observation are count rates in the p–detector (upper panel) and e–detector, respectively. The low detector channels of both detectors can be contaminated by noise events.

Table 9: Weight factors for the count rate errors for each detector channel.

detector	detector channel number															
	1	2	3	4	5	6	7	8	9	10	11	12	13	14	15	16
p–detector	5	3	1	1	1	1	1	1	1	1	1	1	1	1	1	1
e–detector	5	2	1	1	1	1	1	1	1	1	1	1	1	1	1	1

through the inner radiation belt. Further assume the particle flux to have decreased (due to a different path for example) between the first and second passage. Then the peak count rates in the REM detectors are expected to be larger for the first passage than for the second one in both detectors.

Comparing peak count rates of different passages through the radiation belts in both detectors allows to judge the deadtime corrected count rates.

In figure 3.1.5 three examples of deadtime corrected data is shown. Figure 3.1.5a) shows an example with moderate count rates taken on 18 October 1994. The small dip in the e–detector raw count rate curve in the first passage of the outer radiation belt is properly corrected. In both detectors the corrected peak count rates during the first passage of the outer radiation belt are larger than during the second passage.

Figure 3.1.5b) shows an example with very high count rates in the e–detector taken on 17 March 1995. Also in this case the dip in the e–detector count rate curve could be corrected. However the very maximum is undercorrected. The shape of the peak should be as it is detected in the p–detector. Remarkable is the correction of the p–detector count rates. The maximum raw count rate during the second passage of the inner radiation belt is considerably lower than for the other two passages which is not the case for the e–detector count rates. This discrepancy disappears after deadtime correction.

Figure 3.1.5c) shows data of 20 September 1996. Although deadtime correction has become more difficult and uncertain since the testpulser rate has jumped the correction is still useful.

3.2 Deposited doses

Each REM histogram channel corresponds to a range of deposited energy in the detector (see table 2). In table 10 the mean deposited energies are given together with their variance σ_i. The values σ_i have been calculated assuming the ranges given in table 2 to be a measure for the FWHM of the energy–deposit distributions in the different channels. Thus

$$\sigma_i = \frac{E_{dep,i_{max}} - E_{dep,i_{min}}}{2.35} \tag{15}$$

The total deposited energy E_{total} during the accumulation time t_{acc} of one histogram is

$$E_{total} = t_{acc} \cdot \sum_{i=2}^{15} n_{i_{dtc}} \cdot E_{dep,i} \; [keV] \tag{16}$$

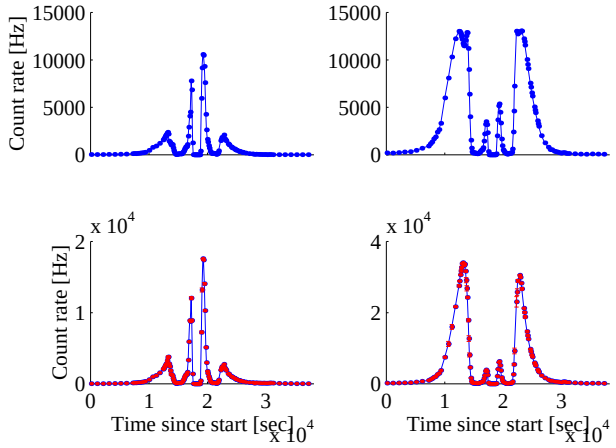

(a)

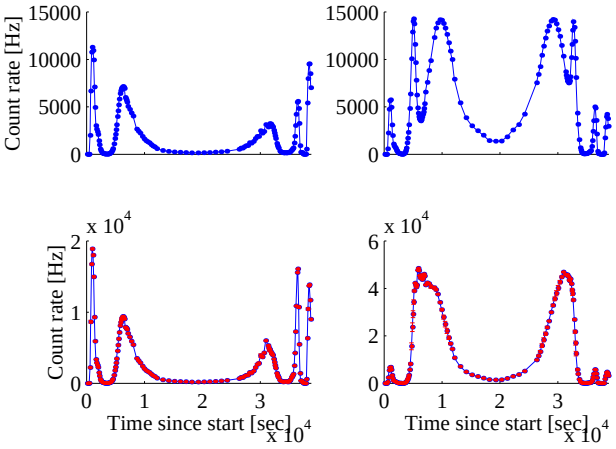

(b)

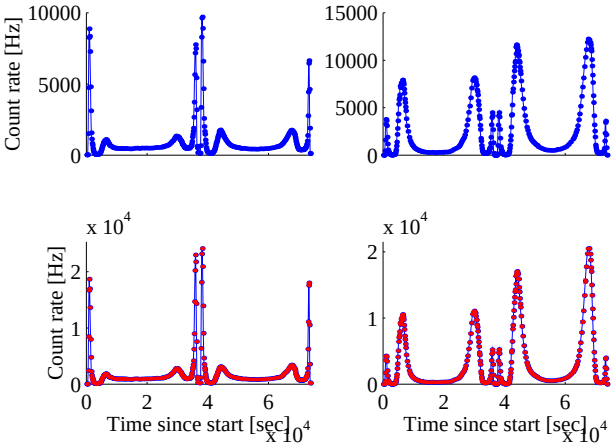

(c)

Figure 12: Three examples of deadtime corrected count rates from 18 October 1994, 17 March 1995, and 20 September 1996. Whereas in the first case (a) with moderate count rates the deadtime could be properly corrected, the peak count rates in the second case (b) with very high count rates is undercorrected. Still after the testpulser rate has jumped in early 1996 the deadtime correction is reliable (c).

Table 10: Measured mean deposited energy E_{dep} $[keV]$ per detector channel and the corresponding variances σ. The values have been calculated from table 2.

	p–detector		e–detector	
Channel	E_{dep}	σ	E_{dep}	σ
1	71.0	6.0	38.5	6.0
2	98.5	6.0	66.0	6.0
3	167.0	23.0	134.0	23.0
4	249.5	12.0	215.0	12.0
5	304.5	12.0	269.0	12.0
6	359.5	12.0	323.5	12.0
7	428.5	18.0	391.5	17.0
8	525.0	23.0	486.5	23.0
9	635.0	23.0	595.0	23.0
10	786.0	41.0	744.0	40.0
11	1046.0	70.0	1004.5	70.0
12	1720.0	217.0	1670.0	213.0
13	4925.0	1147.0	4830.0	1132.0
14	13810.0	2634.0	13645.0	2619.0
15	65000.0	19149.0	64400.0	18979.0
16	>110000.0		>109000.0	

The relation between deposited energy in units of keV and dose in units of rad is given by [5]

$$1[rad] = 6.24 \cdot 10^{10}\ [MeV/kg] \tag{17}$$

The dose D_{total} is obtained by multiplying E_{total} with

$$D_{total} = \frac{E_{total} \cdot 1.6026 \cdot 10^{-5}}{(d \cdot A \cdot \rho_{Si})} \tag{18}$$

where d is the thickness of the silicon diode in μm ($d = 300\ [\mu m]$), A is the detector surface in mm^2 ($A = 150\ [mm^2]$ for the p–detector and and 50 $[mm^2]$ for the e–detector), and ρ_{Si} is the density of the diode material in units of g/cm^3 ($\rho_{Si} = 2.3296\ [g/cm^3]$).

In order to calculate accumulated doses, the doses have to be integrated. Therefore the measured doses are linearly interpolated for the times where no real data measurements are available and the integral is computed using the trapez formula.

3.2.1 Error analysis: deposited doses

From equations (16) and (18) we find:

$$\Delta^2 D_{total} = \frac{1.6026 \cdot 10^{-5}}{(d \cdot A \cdot \rho_{Si})} \cdot t_{acc} \cdot \left[\sum_{2}^{15} \left(\Delta^2 n_{i_{dtc}} \cdot E_{dep,i}^2 + n_{i_{dtc}}^2 \cdot \sigma_i^2 \right) \right] \tag{19}$$

The calculation of $\Delta n_{i_{dtc}}$ has been discussed in section 3.1.4 and the σ_i are given in table 10. The errors of d, A, ρ_{Si}, and t_{acc} are neglected.

3.2.2 Results

In figure 3.2.2 the dose rates and accumulated doses are plotted for an observation on February 27, 1995. The upper two panels are the p–detector doses and the lower two panels the e–detector doses.

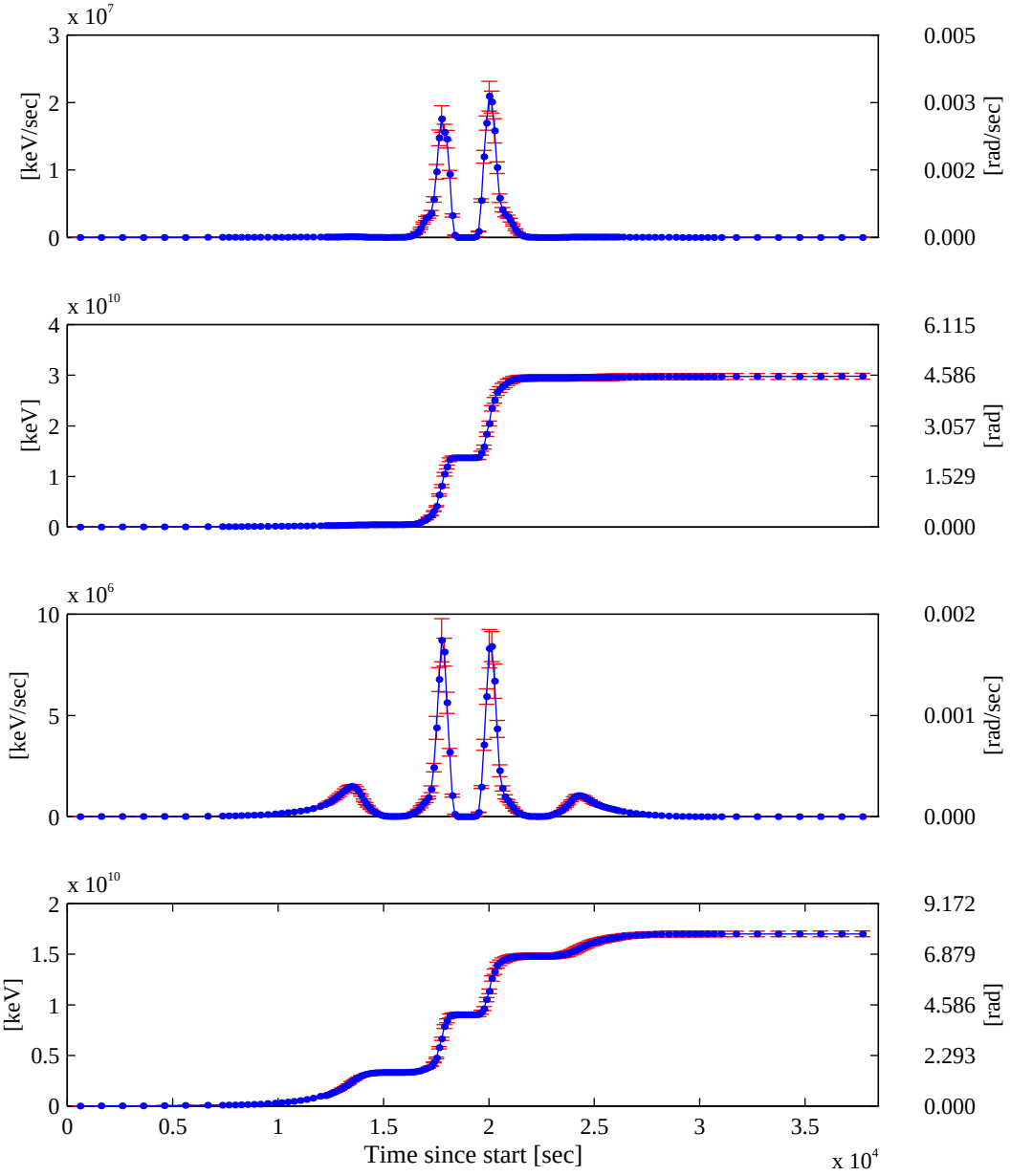

Figure 13: STRV–REM measured dose rate and accumulated doses on February 27, 1995.

3.3 Spectral deconvolution

The particle energy spectra are deduced using equation (6). Therefore the spectra have to be parametrized in some manner and the characterizing parameters found by fitting equation (6) to the observed count rates. Because of the limited energy sensitivity of the instrument the number of fittable parameters and with that the complexity of the model spectra is restricted. The problem can be reduced to a linear one by approximating the spectra by step–like functions: the particle energy spectra are supposed to be piece–wise constant in selected energy intervals. Equation (6) then transforms to

$$\begin{aligned} n_{i_{dtc}} &= \sum_{m=1}^{N_p} f_{p,m} \cdot \int_{E_{p,m}^{min}}^{E_{p,m}^{max}} dE \cdot G_p(E,i) + \sum_{n=1}^{N_e} f_{e,n} \cdot \int_{E_{e,n}^{min}}^{E_{e,n}^{max}} dE \cdot G_e(E,i) \\ &= \sum_{m=1}^{N_p} f_{p,m} \cdot D_{p,m}(i) + \sum_{n=1}^{N_e} f_{e,n} \cdot D_{e,n}(i) \end{aligned} \tag{20}$$

with

$$D_{k,l}(i) = \int_{E_{k,l}^{min}}^{E_{k,l}^{max}} dE \cdot G_k(E,i) \tag{21}$$

N_p is the number of energy intervals the proton spectrum has been divided up and $f_{p,m}$ is the proton flux level in the energy interval $E_{p,m}^{min}$ and $E_{p,m}^{max}$ (correspondingly for electrons: N_e, $f_{e,n}$, $E_{e,n}^{min}$, and $E_{e,n}^{max}$). The linear equation can be written as a matrix equation

$$\vec{n_{dtc}} = \mathcal{D} \times \vec{f} \tag{22}$$

Vector $\vec{n_{dtc}}$ contains the deadtime corrected count rates, $\vec{f}$ is a $N_p + N_e$ element vector of all proton and electron flux levels, and $\mathcal{D}$ a $(N_p+N_e) \times N_{ch}$ element matrix containing the geometric factors integrated over energy in the ranges $E_{k,l}^{min}$, $E_{k,l}^{max}$ (equation (21)). N_{ch} is the number of detector channels used for the deconvolution. The high channels contain very few or no counts and the lowest channels are contaminated by noise and thus not all channels are used for the deconvolution. The selection of the channels is discussed in section 3.3.1.

As $G_k(E,i)$ is only known for the discrete Energy values E_{sim} the integrals in equation (21) are calculated using the trapez formula.
Equation (22) is a so–called linear programming for which dedicated solution algorithms exist [6].

For solving equation (22) we use an iterative non–negative linear least squares method.
Linear least square means to minimize χ^2, the absolute weighted difference between the left and right side in equation (22)

$$minimize \left\| \mathcal{G} \cdot (\vec{n_{dtc}} - \mathcal{D} \times \vec{f}) \right\| \tag{23}$$

The weight matrix $\mathcal{G}$ is a $N_{ch} \times (N_p + N_e)$ diagonal matrix. The elements $\mathcal{G}_{ii}$ are the inverse errors $1/\sigma_i$ of the ith element of the vector $(\vec{n_{dtc}} - \mathcal{D} \cdot \vec{f})$. σ_i is given by

$$\sigma_i^2 = (\Delta n_{dtc_i})^2 + (\Delta[\mathcal{D} \cdot \vec{f}]_i)^2 \tag{24}$$

The Δn_{dtc_i} have been discussed in section 3.1.4. The $\Delta[\mathcal{D} \cdot \vec{f}]_i$ are calculated as follows:

$$\begin{aligned} \Delta^2[\mathcal{D} \cdot \vec{f}]_i &= \Delta^2(\sum_j \mathcal{D}_{ij} \cdot f_j) \\ &= \sum_j \Delta^2 \mathcal{D}_{ij} \cdot f_j^2 \end{aligned} \tag{25}$$

$\Delta\mathcal{D}_{ij}$ is calculated applying simple error propagation to the definition of $\mathcal{D}$ (equation (21)) and using the values of $\Delta G_k(E_{sim}, i)$ discussed in section 2.6.2.

However, in order to calculate the second term in the expression for σ_i (equation (24)) the result of the deconvolution, $\vec{f}$ must be known. As $\vec{f}$ is not know at the beginning the problem must be solved by an iteration process. In the first approach the second term of σ_i is neglected and a first $\vec{f}$ is calculated. In the following iteration steps, the most recent result of $\vec{f}$ is used to compute $\mathcal{G}$. The iteration is stopped when the resulting vector $\vec{f}$ remains constant.

The elements of the result vector $\vec{f}$ can differ by several orders of magnitude. This can cause problems for the algorithm. In order to stabilize the method, the matrix $\mathcal{D}$ is multiplied to the right with a $N_{ch} \times N_{ch}$ diagonal square matrix $\mathcal{H}$, where the elements $\mathcal{H}_{ii}$ are the inverse of the geometric sum of the matrix elements in row i of matrix $\mathcal{D}$. This effects that the elements of the resulting vector $\vec{b}$ are all of the same order of magnitude. The flux levels $\vec{f}$ are finally obtained with $\vec{f} = \mathcal{H} \cdot \vec{b}$. Note that this "trick" does not influence the result. It only makes the algorithm more stable.

The non–negative solving algorithm minimizes the χ^2 under the restriction that all elements of $\vec{f}$ are positive. This is a reasonable restriction, then particle fluxes are always positive.

In figures 3.3 and 3.3 the iteration process is demonstrated on the example of two particular histograms, one taken in the inner belt at $L = 1.64$ and one taken in the outer radiation belt at $L = 4.64$. The series of plots show $\vec{n_{dtc}}$ (red histograms) and $\mathcal{D} \cdot \vec{f}$ (blue histogram) for different iteration steps. From step 2 on $\vec{f}$ remains practically unchanged. However to be sure to have reached the optimal solution always six iteration steps are performed.

3.3.1 Selection of detector channels and Energy bins

As we have seen in section 3.1.3 the count rates in the lowest detector channels can be contaminated by noise. In order to account for this fact the count rate errors have been multiplied with a weighting factor. However, the lowermost channel in both detectors can be totally swamped by noise events and is thus not used for the spectral deconvolution. Channels 15 and 16 contain no useful information for the protons and electrons and are also not used.

Channels 2 to 14 of both detectors are used for the spectral analysis.

The splitting of the energy range into energy bins $E_{k,l}^{min}, E_{k,l}^{max}$ is somehow arbitrary. As the particle spectra are supposed to follow approximately a power law it is reasonable to use energy bins which are equidistant on a logarithmic scale. For the protons the energy is limited to the range between 24 MeV and 600 MeV and divided up into 6 bins. The electrons are restricted

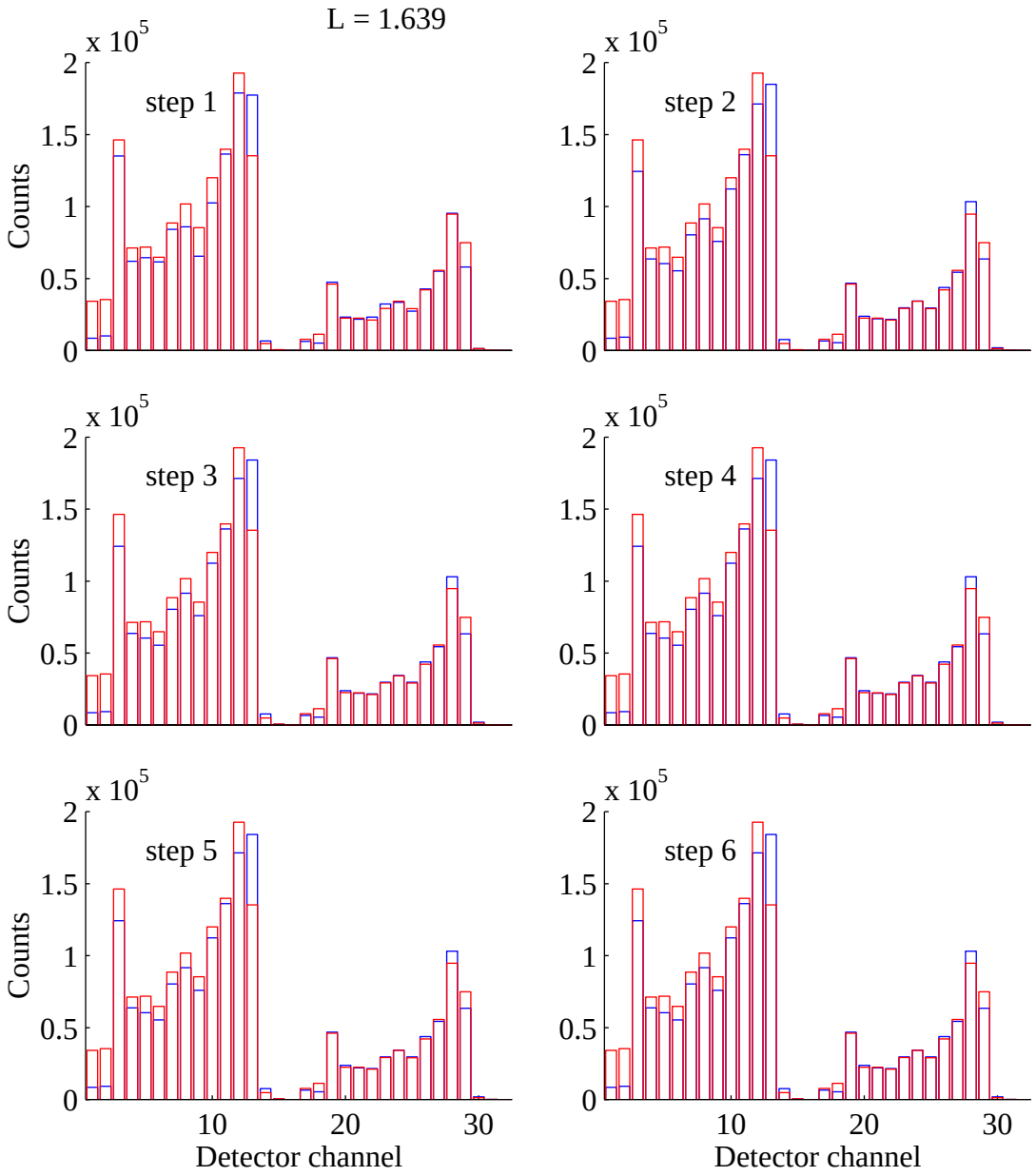

Figure 14: Deconvolution of an accumulation taken in the inner radiation belt. The six panels show the difference between observation and calculation after each iteration step. Blue histograms are observed and red histograms are calculated. After two steps the result remains practically constant.

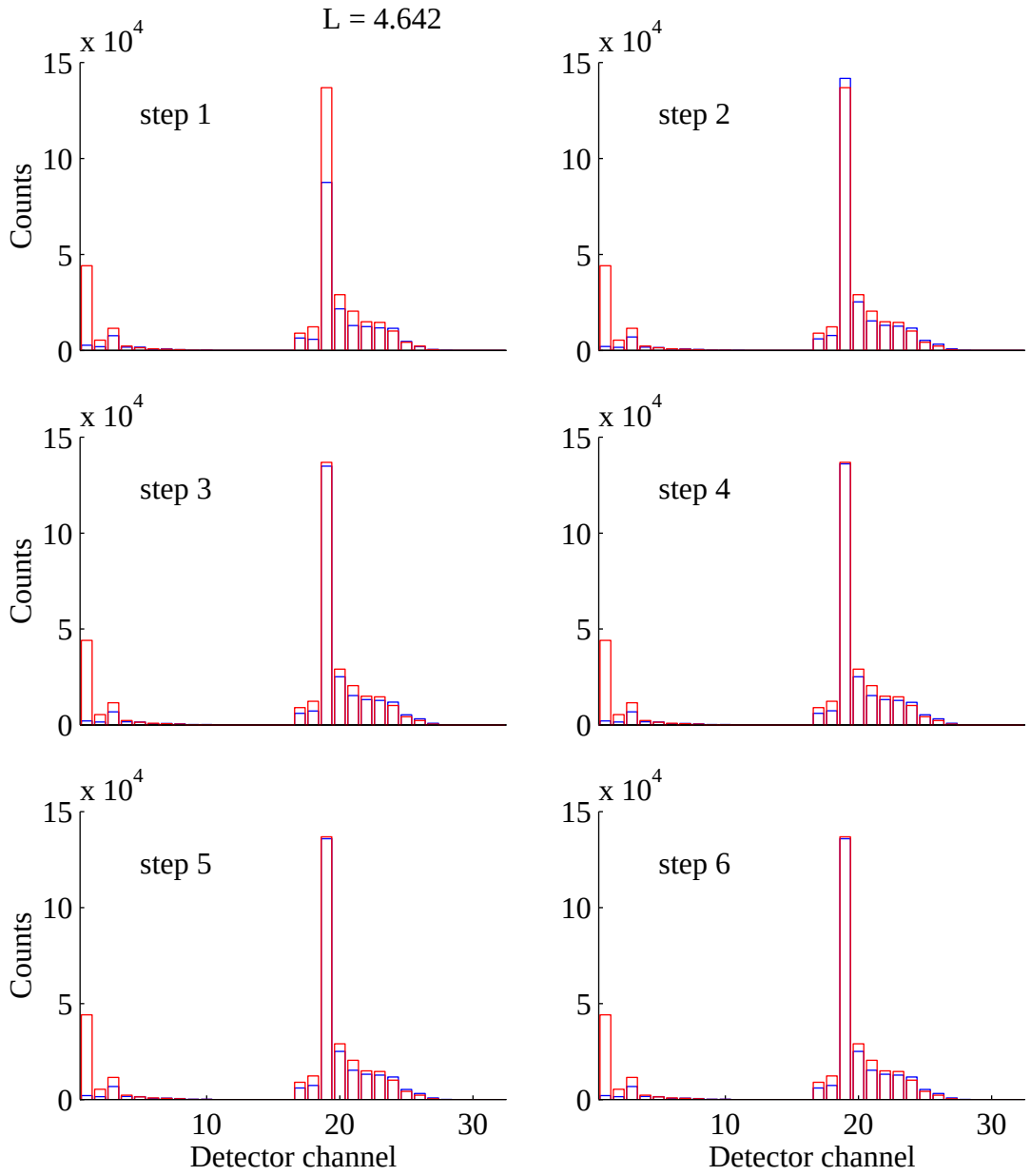

Figure 15: Deconvolution of an accumulation taken in the outer radiation belt. The six panels show the difference between observation and calculation after each iteration step. Blue histograms are observed and red histograms are calculated. After two steps the result remains practically constant.

to energies between 1.2 MeV and 5 MeV and divided up into 3 bins. The such selected energy bins are summarized in table 11.

Table 11: Energy bins $E_{k,l}^{min}, E_{k,l}^{max}$

particle	Energy bins $E_{k,l}^{min}, E_{k,l}^{max}$ $[MeV]$						
k	l						
	1	2	3	4	5	6	7
protons	24.0	40.0	65.0	110.0	175.0	300.0	600.0
electrons	1.2	2.0	3.2	5.0			

3.3.2 Error analysis: spectral deconvolution

The statistical errors of the non–restricted solution f_{min} of the least squares problem (23) can be calculated analytically.

$$\sigma_i(f_{min}) = \frac{\chi^2(f_{min})}{N_p + N_e - N_{ch}} \cdot \left[(\mathcal{D}^T \cdot \mathcal{G} \cdot \mathcal{D})^{-1}\right]_{ii} \tag{26}$$

$\chi^2(f_{min})$ is the χ^2–value of the result vector. Although this formula is not absolutely correct for our non–negative solution we will use it to calculate a good estimate of the flux level errors.

3.3.3 Results

In figure 3.3.3 the deconvolved proton spectra and their errors are plotted for a series of accumulations at L–values between $1.1 < L < 2.7$ taken on November 19, 1994. Figure 3.3.3 shows the electron spectra at L–values between $3.1 < L < 4.3$ from November 19, 1994. The green spectra in the last panels of both figures are the orbital mean AP8/AE8 model spectra [7],[8] calculated for the STRV orbit. Note the good agreement between REM measurements and model calculations, proving the REM results to be very reasonable.

For some of the extracted flux levels the calculated errors are larger than the flux values themselves. For these cases only upper errorbars are drawn. In fact for the highest electron energy bin this is mostly the case!

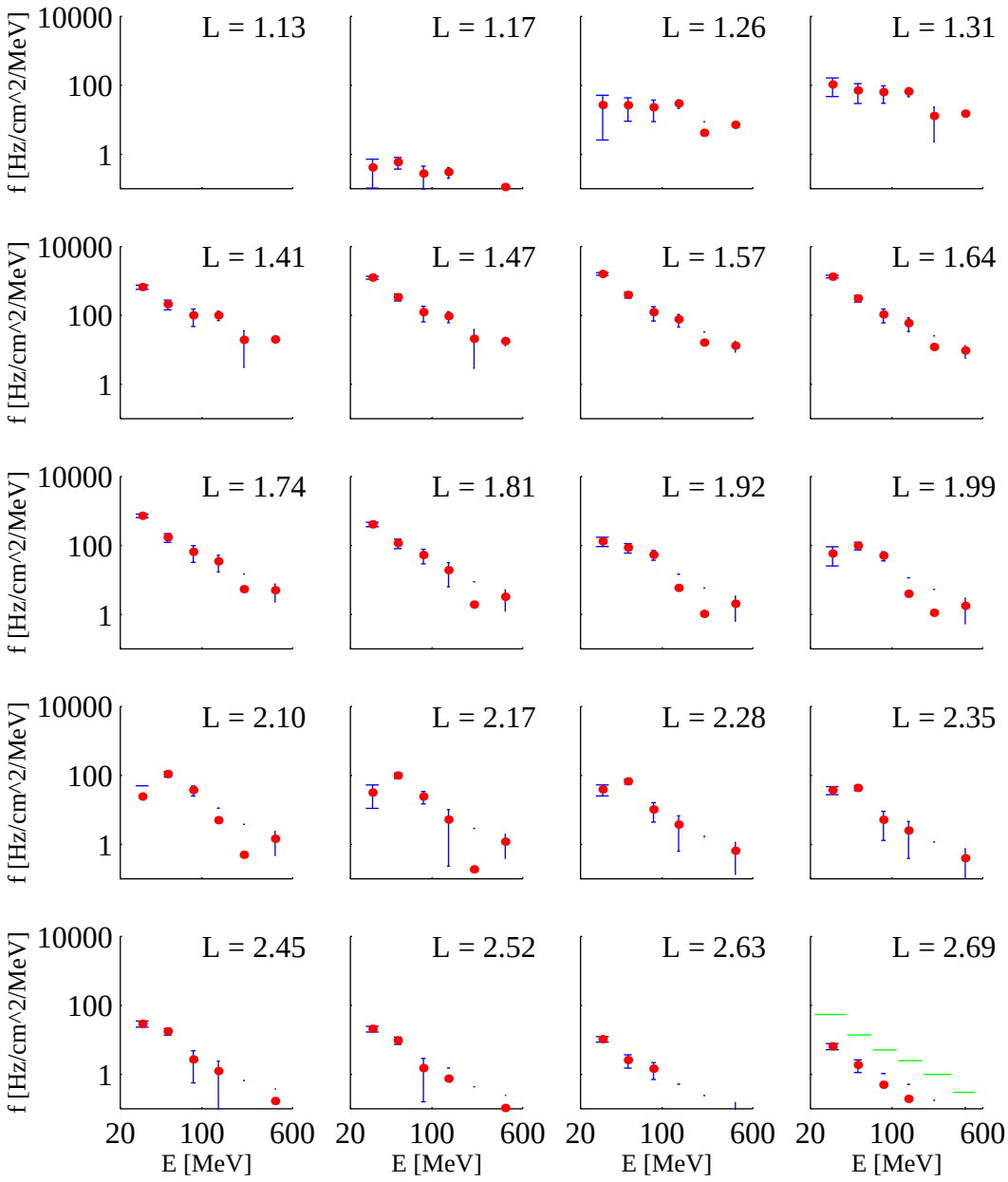

Figure 16: Proton energy spectra at L–shell values between $1.1 < L < 2.7$ on measured with STRV–REM. For comparison the mean AP8 spectrum [7], calculated for the STRV orbit is plotted in the last panel (green histogram). The agreement between measured and modeled flux amplitudes and spectral shapes is very good.

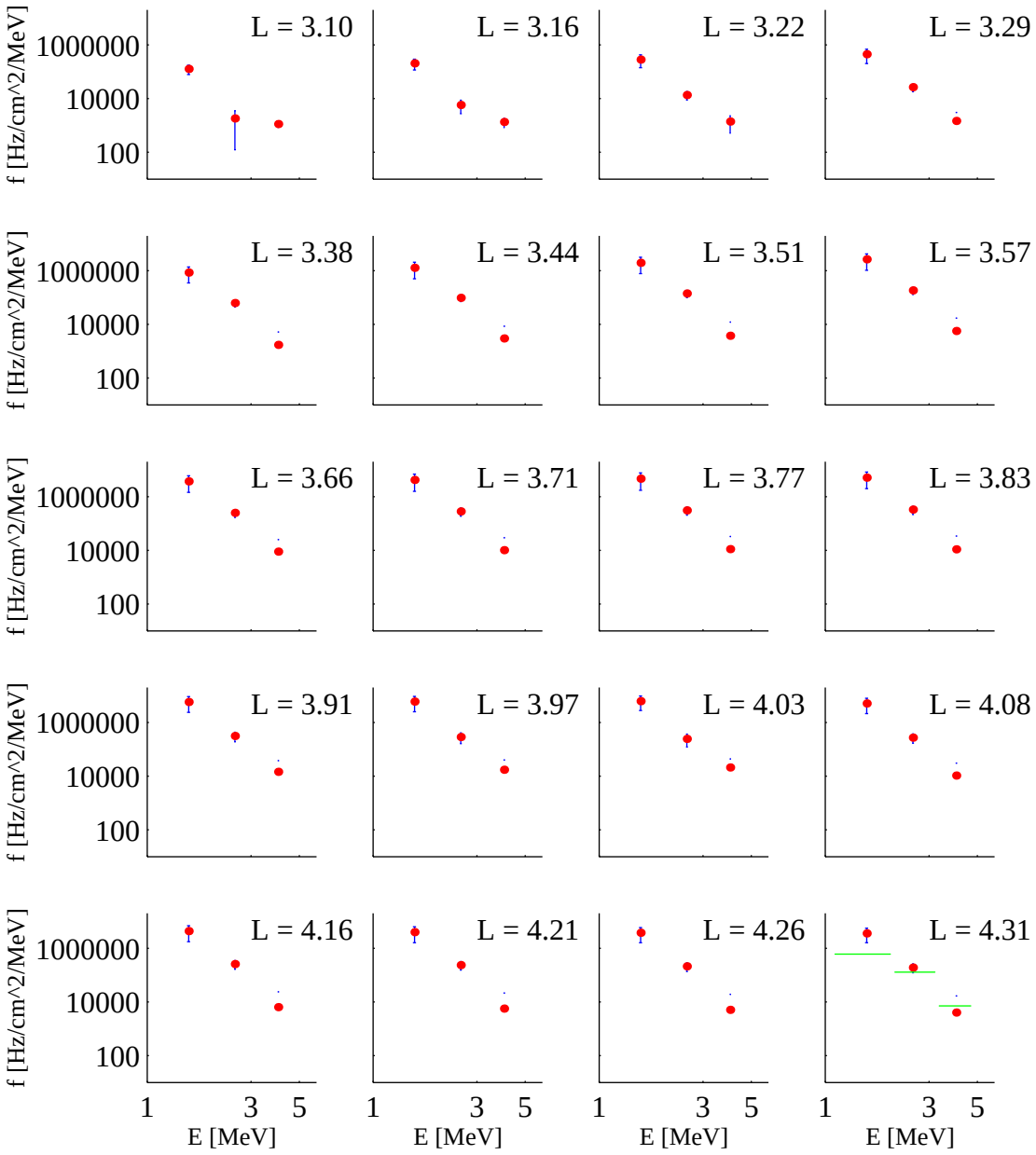

Figure 17: Electron energy spectra at L–shell values between $3.1 < L < 4.3$ on measured with STRV–REM. For comparison the mean AE8 spectrum [8], calculated for the STRV orbit is plotted in the last panel (green histogram). The agreement between measured and modeled flux amplitudes and spectral shapes is very good.

4 Final remarks

The performance of the STRV–REM is constantly changing. The rate of change is strongly related to the activity of the environment. Thus the procedures described in this document must be applied with care to data taken after November 1996. The procedures and the parameters used will have to be checked and reevaluated for coming data.

What can we learn for future instruments?
The fact that the sensitive area of the e–detector is larger than it was assumed to be before launch has caused very high count rates and thus large deadtimes. The deadtime correction has become of great importance. In the case of rapidly varying count rates, e.g. during passages through the inner and outer radiation belts, it is not sufficient to measure the deadtime periodically, as is done with REM. Deadtime must be measured together with the scientific data to allow the proper correction.

During the mission electronic parameters have significantly changed. This complicates the data extraction and increases the errors of the results. There are a few parameters which are essential for the proper functioning of an instrument. These parameters have to be identified during the design phase and special care has to be taken to ensure their stable behaviour throughout the mission. If this is not possible the instrument/electronics have to be designed such that the parameters are allowed to vary in a large range without affecting the performance and logics of the instrument.

References

[1] Janni, J.F. Proton range–energy tables, 1 keV – 10 GeV. *Atomic Data and Nuclear Data Tables*, 27:147, 1982.

[2] Pages, L., Bertel, E., Joffre, H., and Sklaventitis, L. Energy loss and bremsstrahlung yield for 10 keV to 100 MeV electrons in various elements and chemical compounds. *Atomic Data*, 4:1, 1972.

[3] Barraud, C., Duport, Y. Radiation Environment Monitor, TH–V test report for REM–QM/PFM. Technical report, Compagnie Industrielle Radioélectrique SA, June, 1992.

[4] Ljungfelt, S. Software simulation of the REM instrument. PSI internal report, in preparation, 1995.

[5] American Institute of Physics, Particle Group. *Particle Physics Booklet.* American Institute of Physics, 1994.

[6] Lawson, C.L. and Hanson, R.J. *Solving least squares problems.* Prentice–Hall, 1974.

[7] Sawyer, D.M. and Vette, J.I. AP–8 trapped proton environment for solar maximum and solar minimum. Technical report, NSSDC WDC–A–R&S 76–06, NASA–GSFC, 1976.

[8] Vette, J.I. The AE–8 trapped electron model environment. Technical report, NSSDC WDC–A–R&S 91–24, NASA–GSFC, 1991.